Nano Research
https://doi.org/10.1007/s12274-017-1829-3
Research Article
ISSN 1998-0124
CN 11-5974/O4

Ultrathin nanobelts-assembled Chinese knot-like 3D TiO_2 for fast and stable lithium storage

Qili Wu[1], Shiman He[1], Xianfeng Yang[2], Jingling Yang[1], Gaoren Li[1], Yuying Meng[1], Shengfu Tong[1] (✉), Liqiang Mai[3] (✉), and Mingmei Wu[1] (✉)

[1] *MOE Key Laboratory of Bioinorganic and Synthetic Chemistry, School of Chemistry, Sun Yat-Sen University, Guangzhou 510275, China*
[2] *Analytical and Testing Center, South China University of Technology, Guangzhou 510640, China*
[3] *State Key Laboratory of Advanced Technology for Materials Synthesis and Processing, Wuhan University of Technology, Wuhan 430070, China*

Received: 23 June 2017
Revised: 26 July 2017
Accepted: 29 July 2017

KEYWORDS
3D nanoarchitectures,
ultrathin nanobelts,
TiO_2,
lithium ion storage,
ultrahigh rate battery

ABSTRACT

Nanostructured TiO_2 has applications in solar cells, photocatalysts, and fast-charging, safe lithium ion batteries (LIBs). To meet the demand of high-capacity and high-rate LIBs with TiO_2-based anodes, it is important to fine-tune the nanoarchitecture using a well-controlled synthesis approach. Herein, we report a new approach that involves epitaxial growth combined with topotactic conversion to synthesize a unique type of 3D TiO_2 nanoarchitecture that is assembled by well-oriented ultrathin nanobelts. The whole nanoarchitecture displays a 3D Chinese knot-like morphology; the core consists of robust perpendicular interwoven nanobelts and the shell is made of extended nanobelts. The nanobelts oriented in three perpendicular $[001]_A$ directions facilitate Li^+ penetration and diffusion. Abundant anatase/TiO_2-B interfaces provide a large amount of interfacial pseudocapacitance. A high and stable capacity of 130 $mA{\cdot}h{\cdot}g^{-1}$ was obtained after 3,000 cycles at 10 $A{\cdot}g^{-1}$ (50 C), and the high-rate property of our material was greater than that of many recently reported high-rate TiO_2 anodes. Our result provides, not only a novel synthesis strategy, but also a new type of 3D anatase TiO_2 anode that may be useful in developing long-lasting and fast-charging batteries.

1 Introduction

Rocking-chair lithium ion batteries (LIBs), which store and release electrical energy via lithium ion (Li^+) insertion and extraction through the electrode materials, are considered to be the most important and successfully applied energy storage systems [1–5]. Despite possessing advantages such as rechargeability and high energy density [6–8], commercial LIBs with graphite anodes suffer from fatal safety issues. These

Address correspondence to Mingmei Wu, ceswmm@mail.sysu.edu.cn; Shengfu Tong, tongshf@mail.sysu.edu.cn; Liqiang Mai, mlq518@whut.edu.cn

issues are caused by the formation of lithium dendrites due to the batteries' near-zero operating potential and relatively poor cycling stability caused by large volume changes (9%–13%) during lithiation/delithiation [9–12]. Efforts have been made to develop alternative anode materials that would mitigate such safety hazards, promote rate performance, prolong LIB lifespan, and enhance LIB capacity to extend the possible applications of LIBs [13–16]. For example, Yu et al. have designed and synthesized high-energy, high-capacity graphene-based nanostructures, such as vat dye/graphene composites [17], N-doped porous graphene sheets [18], and N, S-codoped graphene [19] for use as LIB anode materials.

Titania (TiO_2), a multifunctional semiconductor, is a promising alternative anode material for LIBs, due to its safe operating potential (~ 1.7 V) and superior cycle stability compared to traditional graphite [1, 20–22]. Various TiO_2 LIBs with competitive electrochemical performances have been reported [23–25]; however, the rate capability of TiO_2 LIBs is unsatisfactory due to their relatively poor conductivity and low Li^+ diffusion coefficient (typically 10^{-8}–10^{-13} $cm^2 \cdot s^{-1}$) [26]. Note that the electrochemical properties of TiO_2 can be adjusted by altering crystal size, morphology, porous properties, and assembly methods [27–30]. Nanostructures with relatively small particle sizes, large surface areas, appropriate pore structures, and diffusion-benefited morphologies are generally useful in reducing ion transfer length and enhancing the electrolyte/electrode contact [29, 31–33].

Thin two-dimensional (2D) TiO_2 nanobelts can supply sufficient active sites on both side surfaces and provide exceptional charge transport properties [29]. It has been shown that nanocrystals (or nanowalls for porous materials) approximately 6.5 nm in size can accommodate the strain that occurs during the spontaneous phase transformation between tetragonal anatase TiO_2 and orthorhombic Li_xTiO_2, resulting in cycling stability improvement [22]. Therefore, 2D nanocrystals constructed into three-dimensional (3D) hierarchical nanoarchitectures are extremely desirable in designing LIB electrode materials that have advantageous properties, such as large surface area, high durability under strain, and negligible aggregation of primary particles [34–37]. Furthermore, the [001] direction of tetragonal anatase TiO_2 improves Li^+ penetration and diffusion [38]. Recently, we rationally synthesized [001]-oriented anatase TiO_2 microcages (*mc*-TiO_2) and hollow nanocubes constructed from [001]-oriented anatase TiO_2 nanoarrays (OATNs), both of which exhibited high rate capacity performances [14, 39]. Therefore, it is necessary to fabricate nanostructured TiO_2 with desirable crystal sizes, architectures, and orientations.

In this study, a nanobelts-assembled 3D TiO_2 nanoarchitecture, constructed of a core composed of robust perpendicular interwoven nanobelts and a shell composed of extended silk-like ultrathin nanobelts, was successfully created from an *mc*-TiO_2 precursor *in situ* [39]. This novel nanoarchitecture maintained the unique 3D perpendicular interwoven assembly of the primary building blocks in the *mc*-TiO_2 precursor. The ultrathin nanobelts, with thicknesses of approximately 6 nm, can supply sufficient active sites of both side surfaces with large surface areas (302 $m^2 \cdot g^{-1}$). As a result, 3D TiO_2 delivers a Li-ion storage capacity of 130 $mA \cdot h \cdot g^{-1}$ after 3,000 cycles at a current of 10 $A \cdot g^{-1}$ (50 C, 1 C ~ 200 $mA \cdot g^{-1}$). The rate capacity and long-cycle stability are superior compared to previously reported TiO_2 nanostructured anodes, such as dispersive TiO_2 nanobelts, *mc*-TiO_2 [39], and TiO_2 microspheres constructed out of ultrathin nanosheets (called AB550) [40]. This novel 3D TiO_2 structure can be utilized in the energy storage and environmental industries, and the synthesis route proposed in this study provides a new strategy for generating new 3D-structured materials.

2 Experimental

2.1 Preparation of 3D TiO_2 nanoarchitectures

3D *mc*-TiO_2 microcages were prepared as reported in our previous work [39]. The *mc*-TiO_2 was used as self-template and hydrothermally treated in 10 M NaOH at 140 °C for a period of time. The product, 3D sodium titanate (NTO), was washed with 1 M acetic acid (HAc), and transformed into 3D hydrogen titanate nanoarchitectures (3D HTO). Finally, 3D TiO_2 nanoarchitectures were obtained by annealing hydrogen titanate in air at 375 °C for 0.5 h. Similar methods were used to prepare randomly dispersed TiO_2 nanobelts with dispersive anatase nanoparticles as precursor.

2.2 Materials characterizations

Powder X-ray diffraction (XRD) patterns were recorded on a Bruker D8 Advance with Cu Kα radiation (40 kV, 40 mA). Rietveld refinement analysis of XRD patterns was used to quantify the abundance of each crystal phase in the samples. The morphology was characterized using an FEI Quanta 400 Thermal Environmental Scanning Electron Microscope (SEM). The structural characterization was conducted using transmission electron microscopy (TEM), high resolution TEM (HRTEM), and scanning transmission electron microscopy (STEM) on a JEOL JEM-2010HR microscope operating at 200 kV and an FEI Tecnai G2 F30 microscope operating at 300 kV. Nitrogen adsorption–desorption isotherms were obtained at 77 K under vacuum on an Autosorb-iQ2-MP (Quanta Chrome).

2.3 Electrochemical measurements

CR2032-type coin half-cells, assembled in a glove box filled with highly purified Ar gas, were used to evaluate electrochemical performance at room temperature. The half-cells consisted of a thin film cathode (working electrode), a lithium foil as the anode, a Celgard 2400 polymer film as the separator, and 1 M $LiPF_6$ (ethylene carbonate (EC): dimethylcarbonate (DMC) = 1:1 in volume) as the electrolyte. The working electrode was composed of an active material (TiO_2), a conductive agent (acetylene black), and a binder material (PVDF) in a mass ratio of 7:2:1. The mass loading of the active material was approximately 0.4–0.7 mg·cm^{-2}. An electrochemical workstation (Autolab PGSTAT302N) was utilized for cyclic voltammetry (0.8–3.0 V) and electrochemical impedance spectra (10^5–0.1 Hz) measurements, while NEWARE testing systems (Neware Co. Ltd, Shenzhen, China) were used in evaluating the galvanostatic discharge/charge performances in the voltage range of 1.0–3.0 V.

3 Results and discussions

3.1 Structure and morphology characterizations

The 3D TiO_2 nanoarchitectures were synthesized directly from 3D *mc*-TiO_2 microcages, which were assembled by the perpendicularly arranged 15 nm anatase nanoparticles, via a self-template method (Fig. S1 in the Electronic Supplementary Material, ESM) [39]. During the transformation, the layered intermediate, NTO, which had a nanobelts-constructed 3D nanoarchitecture (Fig. 1(a)), was obtained via the hydrothermal treatment of *mc*-TiO_2 in a concentrated NaOH solution. The TEM image of the 3D NTO in Fig. 1(a) shows that the nanobelts in this 3D nanoarchitecture are perpendicularly interwoven. Therefore, the 3D arrangement can be preserved during the transformation from *mc*-TiO_2 to 3D NTO due to the analogous zigzag chains of edge-shared TiO_6 octahedra [41]. The nanobelts are interlaced with each other into a rigid cage-like structure in the core and extend outward as flexible silk-like nanoantenna. Such a morphology gives the nanoarchitecture high mechanical stability and enhanced contact with between neighboring structures, as shown by the SEM images in Fig. S2 in the ESM. The selected area electron diffraction (SAED) pattern of the 3D NTO (Fig. 1(b)) has four bright and broad diffraction spots that form a square, which can be assigned to $(200)_N$ planes of 3D NTO (subscript N is denoted as 3D NTO). The nanobelts are approximately 1 μm in length and 6 nm in thickness (nearly 8 layers) with a lattice spacing of 0.76 nm as indicated in the HRTEM image (Figs. 1(c) and 1(d)), which further confirms the layered crystal structure and ultrathin dimensionality of the nanobelts. Through substituting H^+ for Na^+ by washing 3D NTO with HAc (Fig. 1(e)), 3D HTO nanoarchitectures were readily obtained *in situ* via a topotactic ion-exchange process. Typical XRD patterns of the 3D NTO and 3D HTO are shown in Fig. S3 in the ESM. Considering that both NTO and HTO have identical lepidocrocite-type framework structures, the crystal data of $H_2Ti_2O_5{\cdot}H_2O$ (PDF#47-0124, a = 0.3784 nm, b = 1.803 nm, and c = 0.2998 nm) is used hereafter to be representative of NTO [41–44]. A vertical view of the sample, as shown in Fig. 1(a), suggests that the rigid cage-like core connected to extended nanobelts can be summarily described as a 2D Chinese knot. The ultrathin nanobelts-assembled nanoarchitecture of 3D NTO (or 3D HTO) is schematically illustrated in Fig. 1(f) to show the nanobelts' perpendicular organization in three dimensions, and the model is similar in shape to a 3D Chinese knot (Fig. 1(g)).

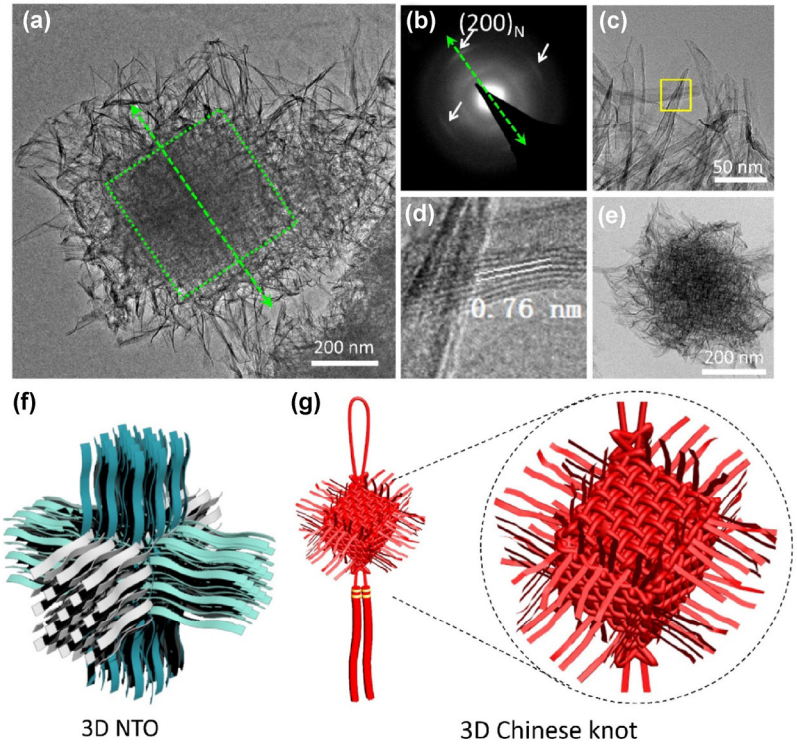

Figure 1 Morphologies of 3D NTO and HTO. (a) Low magnification TEM image of 3D NTO nanoarchitecture, and (b) the corresponding SAED pattern. (c) HRTEM image of the nanobelts. (d) The HRTEM image of the cubic area marked in (b). (e) Low magnification TEM image of a 3D hydrogen titanate (HTO) nanostructure converted from the 3D NTO nanoarchitecture. (f) A 3D model of the 3D NTO. The three different colors denote the three orientations of the nanobelts. (g) A 3D Chinese knot.

After annealing 3D HTO at 375 °C for 0.5 h, anatase phase 3D TiO_2 nanoarchitectures (3D TiO_2) with minor TiO_2-B were obtained, as shown by the XRD pattern and corresponding Rietveld refinement results (Fig. S4 in the ESM). As presented in the TEM images in Figs. 2(a) and 2(b), and the STEM image in Fig. S5(a) in the ESM, the TiO_2 morphology inherits the unique 3D nanoarchitecture from 3D HTO (Fig. 1(c)).

An apparent crystallographic orientation of anatase nanocrystals is observed from the SAED pattern in Fig. 2(c). The discrete inner diffraction ring can be assigned to the $(101)_A$ planes of anatase (subscript A denotes anatase), while the two bright and elongated diffraction spots correspond to the $(200)_A$ plane. In addition, the line connecting the bright diffraction spots in Fig. 2(c) is parallel to the elongation direction of the nanobelts in Fig. 2(a), thus indicating that the $[100]_A$ direction is along the nanobelt. A similar phenomenon is also observed in 3D NTO nanobelts (Fig. 1(a)). A detailed description of the transformation mechanism will be discussed in the next section. The SAED data indicate that the numerous anatase nanocrystals throughout the entire nanoarchitecture are oriented in order, as shown by the model in Fig. 2(d). Note that the 3D nanostructures with three orientations are preserved throughout our multiple-topotactic conversion process. The HRTEM image of the nanobelt in Fig. S5(b) in the ESM displays the lattice fringes of anatase in the $(01\bar{1})_A$ and $(002)_A$ planes, indicating that the material has a high degree of crystallinity. Our sample also has a large Brunauer–Emmett–Teller (BET) surface area of 302 $m^2 \cdot g^{-1}$ with a pore size of approximately 10 nm (Fig. 2(e)). The ultrathin nanobelts do not only facilitate Li^+ transport by shortening the ion diffusion distance, but they also supply more surface active sites, and their large surface areas provide efficient electrolyte/electrode contact as well. Importantly, the strain of transforming between the anatase (phase A) and the orthorhombic Li_xTiO_2 structures (phase B) is accommodated within

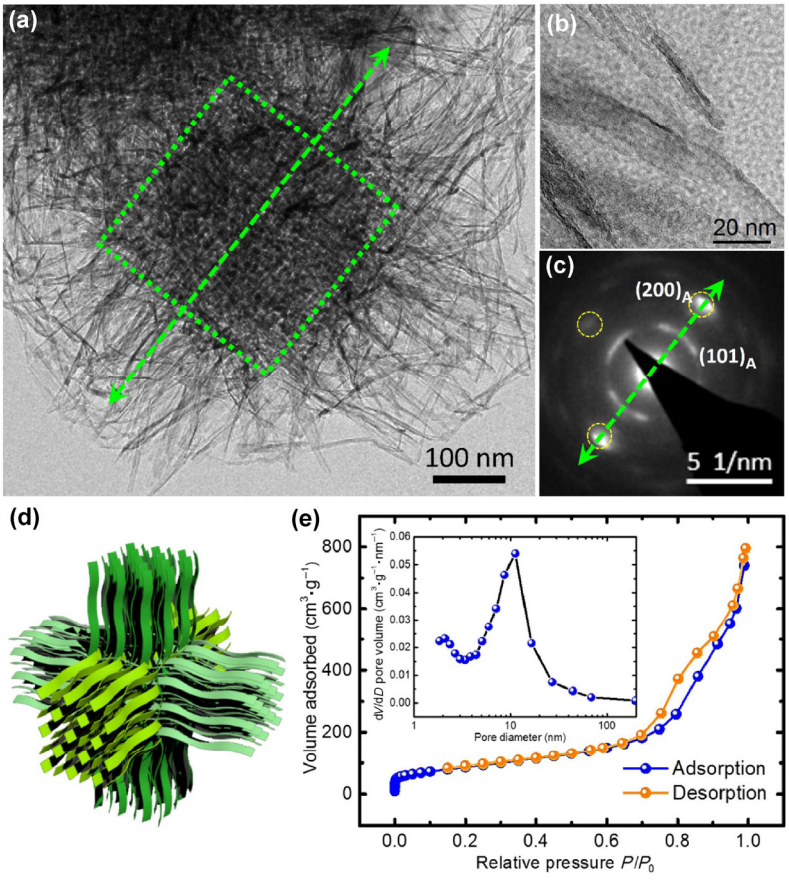

Figure 2 Morphology of 3D TiO_2 transformed from 3D HTO. Low (a) and high (b) magnification TEM images, and the corresponding SAED pattern (c). (d) A 3D model. Three different colors denote three special orientations of the nanobelt branches. (e) Nitrogen adsorption and desorption isotherm of 3D TiO_2. Inset is the pore size distribution.

the thin belts through intercalation [22, 31]. Hence, we predict that the as-prepared TiO_2 nanoarchitecture will have excellent Li^+ storage performance as an anode material.

3.2 Conversion mechanism

Based on the TEM results and the crystal structures of anatase TiO_2 and NTO, a conversion mechanism from nanoparticles-assembled 3D *mc*-TiO_2 to nanobelts-assembled 3D NTO, and finally to 3D TiO_2 was proposed, as shown in Schemes 1 and 2. The anatase phase has a tetragonal structure with unit cells $a = b \neq c$ due to the discrepancy in length of Ti–O bonds along and across the $[001]_A$ direction, i.e., 0.198 and 0.194 nm (Scheme 1(a)), respectively. When hydrothermally treated in 10 M NaOH solution, the primary anatase nanoparticles in the *mc*-TiO_2 are delaminated into tiny planar Ti-O fragments along the $[001]_A$ direction and form small NTO nanoplates with $[010]_N//[001]_A$ (see Schemes 1 and 2(b)). Then, these small NTO nanoplates connect with each other along the *ac* plane, becoming longer NTO nanobelts (Scheme 2(c)) [45–48]. Note that a *mc*-TiO_2 microcage is constructed by anatase nanoparticles oriented in three perpendicular directions, and all six faces of the microcage are dominated by $[001]_A$ facets [39]. Consequently, the delamination takes place in three perpendicular directions (see Scheme 2(d)). Primary anatase nanoparticles aligning in one specific orientation will be delaminated along the same direction, as shown in Scheme 2(b). Due to the bondage of the primary perpendicular interwoven structure of *mc*-TiO_2, the NTO nanobelts are unable to move freely, but are arranged in parallel along the $[100]_N$ directions. Conversely, the epitaxially grown nanobelts extended outward are quite flexible.

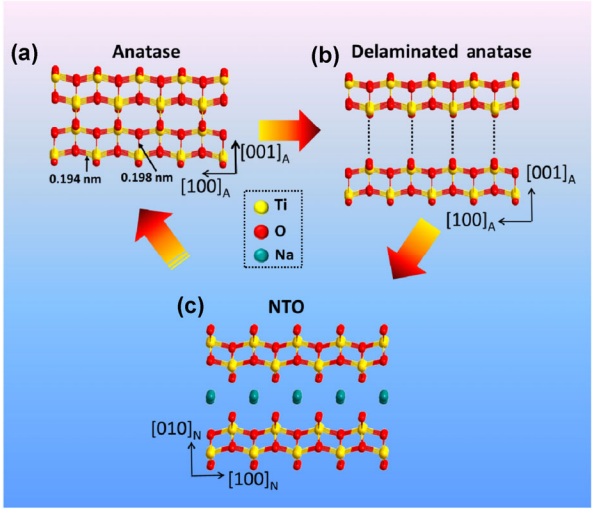

Scheme 1 Atomic models of the phase conversions. (a) Anatase along the $[001]_A$ direction. (b) The anatase was delaminated along the $[001]_A$ direction by breaking the long Ti–O bonds in (a). (c) NTO layer structure model along the $[010]_N$ direction.

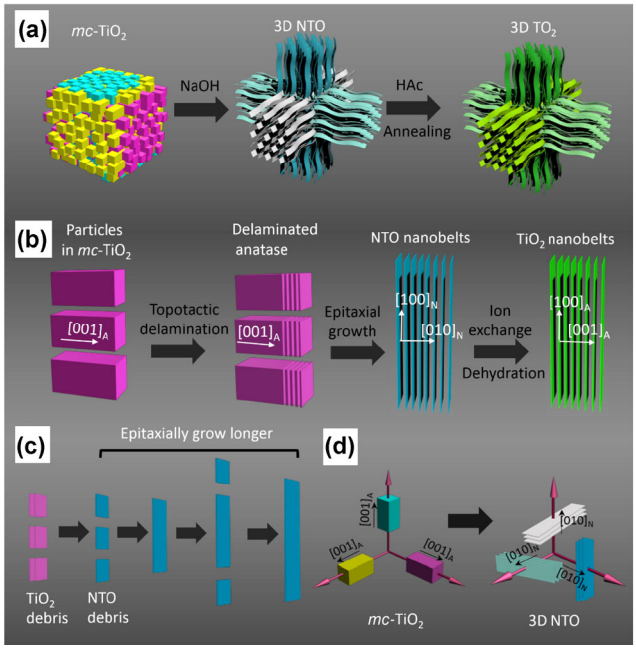

Scheme 2 Schematics of the transformation process and mechanism. (a) An overview of the transformation from the *mc*-TiO_2 to 3D NTO, and then to 3D TiO_2 nanoarchitectures. (b) Nanoparticles in *mc*-TiO_2 (violet) undergo topotactic delamination and epitaxial growth to form NTO nanobelt arrays, and finally become TiO_2 nanobelt arrays. (c) Details of the epitaxial growth process in (b). (d) 3D crystallographic orientation relationships between the anatase nanoparticles in *mc*-TiO_2 and nanobelts in 3D NTO.

We conducted time-dependent control experiments (Fig. S6 in the ESM) to confirm that the delamination process starts from outside of the microcage and proceeds inward. The entire microcage can be completely delaminated to a completely nanobelts-constructed 3D nanoarchitecture after a 6-h reaction (Fig. 1). Regardless of the fabrication conditions, most reported sodium titanate nanotubes or nanoplates obtained via the alkaline hydrothermal method have similar thicknesses of 3–8 nm [49–51]. After the delamination and transformation processes, we confirmed that the thicknesses of our NTO nanobelts also fell within this range. With the ion exchange between Na^+ and H^+ (or H_3O^+), the lepidocrocite-type framework structure can be well preserved and the ultrathin nanobelts (with thicknesses of approximately 6 nm) can be inherited [52–54]. Upon annealing, the layered HTO with a lepidocrocite-type framework structure will revert back to the anatase phase. During this process, the nanobelts-assembled 3D nanoarchitecture persists due to its mimicking of the TiO_6 zigzag chain [41]. In short, the *mc*-TiO_2 microcage precursor can be converted to a 3D Chinese knot-like TiO_2 architecture, during which the 3D orientations of the building units (nanocrystallites to nanobelts) are well preserved (Scheme 2(a)).

3.3 Li ion storage performances

The electrochemical properties of the obtained 3D hierarchal nanobelt TiO_2 for Li-ion storage is fully described in this section, and a comparison of the electrochemical performance between the product in this study and the pristine *mc*-TiO_2 precursor is also discussed. Figure 3(a) shows the cyclic voltammograms (CVs) of the 3D TiO_2 nanoarchitecture-composed lithium half-cell at a scan rate of 0.1 $mV \cdot s^{-1}$. Two primary redox peaks at 1.7 and 2.0 V originate from the lithiation/delithiation of anatase [55, 56], while the two pairs of weak redox peaks between 1.5 and 1.7 V correspond to a small amount of TiO_2-B in the material [57]. Some additional broad peaks between 0.8 and 1.5 V that were observed in the first cycle and disappeared in subsequent cycles, can be attributed to irreversible reactions [58–60]. The second and third cycles highly overlap, thus confirming a stable storage and release of Li^+ in subsequent cycles. The galvanostatic discharge/charge curves of the initial five cycles and the one-hundredth cycle at a current density of

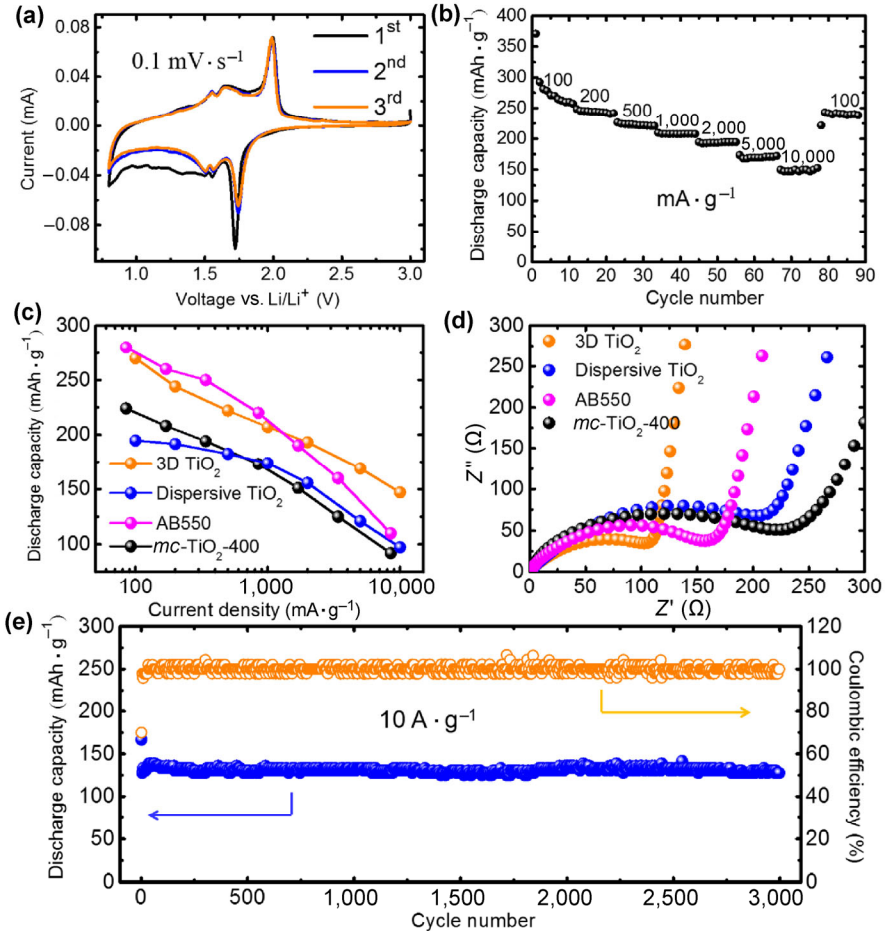

Figure 3 Li-ion storage properties. (a) Representative CV curves of 3D TiO_2 nanoarchitectures at a scan rate of 0.1 $mV·s^{-1}$ for the initial three cycles. (b) Rate capability at various current densities. (c) Comparison of capacities of 3D TiO_2 nanoarchitectures, dispersive TiO_2 nanobelts, and previously reported AB550 [12] and *mc*-TiO_2-400 [11] at various current rates. (d) Electrochemical impedance spectra (Nyquist plots) of fresh electrodes at open circuit potentials. (e) Long-term cycling performance and coulombic efficiency of 3D TiO_2 nanoarchitectures at a high current density of 10 $A·g^{-1}$.

100 $mA·g^{-1}$ (0.5 C) are shown in Fig. S7(a) in the ESM. These curves can be divided into three lithiation steps, including a homogeneous lithium insertion into the bulk stage, a biphasic (Li-rich and Li-poor phases) plateau, and an interfacial lithium storage step, which is similar to a phenomenon reported previously [32, 40]. The interfacial lithium storage can be attributed to the anatase/TiO_2-B interfaces, as discussed in our previous work [40]. During the first cycle, the discharge capacity reached approximately 350 $mA·h·g^{-1}$, while the charge capacity was approximately 247 $mA·h·g^{-1}$, resulting in an efficiency of 70.5%. This relatively low coulombic efficiency can be attributed to the small size of the nanobelts which induces surface side reactions and partially irreversible capacity loss [61]. In subsequent cycles, the coulombic efficiency increased and reached approximately 100%, indicating that the electrode stabilized, which is consistent with our CV measurements. Since the theoretical capacities of anatase and TiO_2-B are 170 and 335 $mA·h·g^{-1}$, respectively, the theoretical capacity of 3D TiO_2 can be calculated to be 170 × 83.2% + 335 × 16.8% ≈ 200 $mA·h·g^{-1}$. The capacities of initial five cycles were larger than the theoretical value, which could be due to surface side reactions and extra interfacial lithium storage at the anatase/TiO_2-B interfaces. The capacity slightly decreased during the initial 20 cycles and then stabilized to a value of 194 $mA·h·g^{-1}$ (Fig. S7(b) in the ESM). The stable capacity of 3D TiO_2 at 100 $mA·g^{-1}$ (0.5 C) and the calculated theoretical capacity are

nearly equivalent.

Figure 3(b) shows the rate capabilities of the 3D TiO_2 nanoarchitecture as a function of current density from 100 $mA·g^{-1}$ (0.5 C) to 10 $A·g^{-1}$ (50 C). The average capacities are 270, 244, 222, 207, 193, 169, and 147 $mA·h·g^{-1}$ at corresponding current densities as indicated in the figure. The pseudocapacitance of TiO_2(B) and the interfacial storage of anatase/TiO_2-B show an increasingly dominant role at high rates [32, 40]. Therefore, the contributions of capacitive effects and diffusion-controlled reactions in the 3D TiO_2 material at different current densities were investigated using CV experiments. The CV curves, obtained at scan rates from 0.1 to 1 $mV·s^{-1}$, and the corresponding results are shown in Fig. S8 in the ESM, and were determined using Eq. (1) [62]

$$i(V) = k_1 v + k_2 v^{1/2} \quad (1)$$

where $k_1 v$ and $k_2 v^{1/2}$ correspond to the current contributions from surface capacitive effects and the diffusion-controlled reactions, respectively. As predicted, the contribution of capacitive effects (red) increased with increased scan rate, from 73.2% at 0.1 $mV·s^{-1}$ to 91.2% at 1.0 $mV·s^{-1}$, indicating that the pseudocapacitance plays a more significant role in fast lithium storage. For comparison, dispersive TiO_2 nanobelts were synthesized by a similar method with dispersive anatase nanoparticles as a precursor (Fig. S9 in the ESM). A comparison of the rate capabilities of the 3D TiO_2 nanoarchitecture material, dispersive TiO_2 nanobelts, *mc*-TiO_2-400 (obtained by annealing *mc*-TiO_2 at 400 ℃ for 2 h) [39], and AB550 (anatase/TiO_2-B nanosheet-constructed microspheres) [40] is shown in Fig. 3(c). The 3D TiO_2 nanoarchitecture displays higher rate capabilities than TiO_2 nanobelts and *mc*-TiO_2-400. Additionally, the 3D TiO_2 nanoarchitecture material also has capacities superior to those of AB550 when the current density is above 1 $A·g^{-1}$ (5 C), indicating that the 3D TiO_2 nanoarchitecture has better capacity retention and superior high rate capabilities during fast charge and discharge. This superiority is due to the 3D TiO_2 nanoarchitecture with a unique core–shell and $[001]_A$ oriented structure, abundant anatase/TiO_2-B interfacial lithium storage, and the ideal thickness (approximately 6 nm) of the nanobelts, which results in enhanced surface contact area, the ability of the material to accommodate strain caused by the penetration and transport of Li^+, shortened Li^+ diffusion length, and improved charge transport properties.

The BET surface areas and pore size distributions of the three controlled samples were estimated based on their nitrogen adsorption–desorption isotherms, as displayed in Fig. 2(e), Fig. S10 and Table S1 in the ESM. The BET surface areas of 3D TiO_2, AB550, *mc*-TiO_2-400, and dispersive TiO_2 nanobelts are 302, 62.3, 79.1 and 247 $m^2·g^{-1}$, respectively, and 3D TiO_2 has the largest surface area apparently. While the dispersive TiO_2 nanobelts have a similar surface area and pore structure to that of 3D TiO_2, their inferior performance can be explained by their random arrangement compared to well-ordered architecture of 3D TiO_2. The alternative current (AC) electrochemical impedance analysis was also carried out on the half-cells of these four materials to estimate the extrapolations, and the corresponding impedance Nyquist spectra are presented in Fig. 3(d). All these electrodes have comparable Nyquist plots with a depressed semicircle and an oblique line in the high and low-frequency ranges, respectively. We used an equivalent circuit (Fig. S11 in the ESM) to analyze the electronic interfacial parameters of the half-cells [63, 64]. Herein, R_b represents the resistance of the electrolyte, separator, and electrode. C_1 and R_1 value the effects of conductivity, electrode roughness, and inhomogeneous reactions at the material surface. R_{ct} is the charge transfer resistance between the electrolyte and electrode at the TiO_2 anode surface; Z_w is the Warburg resistance related to charge diffusion. The resultant values calculated based on the equivalent circuit are listed in Table S2 in the ESM. All these samples have similar R_b values (1–2 Ω), while the 3D TiO_2 nanoarchitecture exhibits the smallest R_1 (12.2 Ω), R_{ct} (61.8 Ω) and Z_w (120 Ω) values. Lithium diffusion coefficients in the four samples were also calculated based on the EIS results, as explained in the ESM [64, 65]. These results, shown in Figs. 3(b) and 3(c), strongly support the conclusion that 3D TiO_2 nanoarchitecture offers improved electronic conductivity, electrolyte contact, and pseudocapacitance contribution at high rates.

Compared to other recently reported TiO_2 nanostructures, the 3D TiO_2 material, without any further modifications, demonstrates high-quality electrode performance. This material has higher capacities than many carbon or graphene composited TiO_2 and doped TiO_2 nanostructures [21, 66–69]. The anatase-dominated 3D TiO_2 delivers comparable rate capacities to those reported for TiO_2-B ultralong nanotubular materials [57]. Generally, TiO_2-B with a layer structure possesses open channels that facilitate greater Li^+ mobility, and the theoretical specific capacity of TiO_2-B is 335 $mA{\cdot}h{\cdot}g^{-1}$ (corresponding to $LiTiO_2$ as a final lithiated product), which is higher than that of anatase TiO_2 (~ 170 $mA{\cdot}h{\cdot}g^{-1}$). Therefore, it is worth noting that creating anatase-dominated 3D TiO_2 with comparable capacities to that of pure phase TiO_2-B is a great achievement. As seen in Fig. S12 in the ESM, the excellent performance of 6-nm anatase nanoparticles further confirms that a dimension of 6 nm provides satisfactory electron pathways [22, 31]. C-doped TiO_2 multiple-phase nanocomposites (anatase, TiO_2-B and TiC) [68], exhibited the highest capacities due to their enhanced conductivity as a result of carbon doping. Nevertheless, the approach of utilizing multiple phase interfaces in the C-doped TiO_2 multiple-phase nanocomposite is consistent with our material design methodology, confirming that our strategy is appropriate for designing nanomaterials suitable for use in high-performance LIBs.

The long-cycle stability of our 3D TiO_2 nanoarchitecture electrode system was evaluated. Figure 3(e) shows the discharge capacity and coulombic efficiency at a current density of 10 $A{\cdot}g^{-1}$ (50 C) up to 3,000 cycles. The electrode exhibits a high initial capacity of 166 $mA{\cdot}h{\cdot}g^{-1}$ and a terminal capacity of 130 $mA{\cdot}h{\cdot}g^{-1}$ (with a retention of 76.5%) for over 3,000 cycles with approximately 100% coulombic efficiency after several initial cycles. The discharge/charge curves of 3D TiO_2 at 10 $A{\cdot}g^{-1}$ (50 C) at the 1st, 1,000th, 2,000th, and 3,000th cycles in Fig. S13 in the ESM exhibit the same curve shape and specific capacity, confirming a stable charge/discharge process. The first cycle has a lower coulombic efficiency and larger discharge/charge potential difference than the rest cycles because the electrode undergoes an activation process at high current density and displays a stable discharge/charge performance over the remaining thousands of cycles. Compared to the reported TiO_2 nanostructures (see details in Table S3 in the ESM), our 3D TiO_2 electrode shows outstanding long-term stability and capacity retention, especially at high rates (in this case 10 $A{\cdot}g^{-1}$ or 50 C). Few reported TiO_2 nanostructures are capable of maintaining a comparably high and stable capacity, as well as capacity retention at such a high current density. Moreover, after 1,000 cycles at 1 $A{\cdot}g^{-1}$ (5 C), the nanobelt morphology in 3D TiO_2 is still preserved (Fig. S14 in the ESM), which suggests that 3D TiO_2 is structurally stable. This result further proves that this unique nanoarchitecture with robust 3D perpendicular interwoven nanobelts can effectively uphold the structural integrity of the electrode during repeated cycles. It is believed that the nanobelts in this material can accommodate the strain during the spontaneous phase transformation between tetragonal anatase TiO_2 and orthorhombic Li_xTiO_2 during lithiation/delithiation, which allows for consistent cycling stability [22]. All these results imply that our unique nanobelts-assembled 3D TiO_2 material is suitable for use in high-capacity and long-lasting LIB anodes, especially for high-rate (fast charging) applications.

4 Conclusion

In summary, a new type of 3D TiO_2 nanoarchitecture, constructed by ultrathin and well-oriented nanobelts has been successfully synthesized from a TiO_2 microcage (*mc*-TiO_2) self-template, through a combined epitaxial growth and topotactic conversion approach. The obtained 3D TiO_2 is composed entirely of nanobelts arranged in a core-branch morphology, resembling a 3D Chinese knot. The rigid core effectively enhances the mechanical stability of the material, while the flexible shell nanobelts can offer sufficiently large surface areas to interact with an electrolyte and the adjacent nanoarchitectures effectively. The $[001]_A$ orientation of the nanobelts in three perpendicular directions facilitates the penetration and fast transport of Li^+. As a result, the 3D TiO_2 electrodes showed excellent rate capability and cycling stability with a high and stable capacity of 130 $mA{\cdot}h{\cdot}g^{-1}$ at a current density of 10 $A{\cdot}g^{-1}$ (50 C) after 3,000 cycles. Therefore,

the unique orientation of the ultrathin nanobelts-assembled 3D TiO_2 nanoarchitecture is well-suited to the application of fast-charging LIBs.

Acknowledgements

This research was supported financially by the National Natural Science Foundation of China (NSFC) (Nos. 51672315, U1301242, 21271190, and 21403106), the government of Guangzhou city for an international joint-project (No. 201704030020), the Government of Guangdong Province for NSF (No. S2012020011113) and the provincial Ministry of Cooperative funded special funds (Nos. 2013A090100010, 2016B090932005, and 2015B090927002), the Fundamental Research Funds for the Central Universities (No. 16lgpy18). The authors acknowledge Prof. Hong Jin Fan from Nanyang Technological University for helpful discussions.

Electronic Supplementary Material: Supplementary material (SEM, TEM, XRD patterns, nitrogen adsorption and desorption curves of the precursor and products, discharge/charge curves of the 3D TiO_2, CV curves of 3D TiO_2 at various scan rates, and the comparison of electrochemical performances of 3D TiO_2 with that of previously reported TiO_2-based materials) is available in the online version of this article at https://doi.org/10.1007/s12274-017-1829-3.

References

[1] Zhu, G. N.; Wang, Y. G.; Xia, Y. Y. Ti-based compounds as anode materials for Li-ion batteries. *Energy Environ. Sci.* **2012**, *5*, 6652–6667.

[2] Liu, X. F.; Tong, S. F.; Dai, C. G.; He, P.; Zhou, H. S. Synthesis of quasi-spherical micro-size lithium titanium oxide by an easy sol-gel method. *J. Solid State Electrochem.* **2015**, *19*, 299–305.

[3] Bruce, P. G.; Scrosati, B.; Tarascon, J. M. Nanomaterials for rechargeable lithium batteries. *Angew. Chem., Int. Ed.* **2008**, *47*, 2930–2946.

[4] Goodenough, J. B.; Kim, Y. Challenges for rechargeable Li batteries. *Chem. Mater.* **2010**, *22*, 587–603.

[5] Balogun, M.-S.; Qiu, W. T.; Luo, Y.; Meng, H.; Mai, W. J.; Onasanya, A.; Olaniyi, T. K.; Tong, Y. X. A review of the development of full cell lithium-ion batteries: The impact of nanostructured anode materials. *Nano Res.* **2016**, *9*, 2823–2851.

[6] Wang, Y. H.; Zeng, J. R.; Cui, X. Q.; Zhang, L. J.; Zheng, G. F. Separator-integrated, reversely connectable symmetric lithium-ion battery. *Small* **2016**, *12*, 1091–1097.

[7] Larcher, D.; Tarascon, J. M. Towards greener and more sustainable batteries for electrical energy storage. *Nat. Chem.* **2015**, *7*, 19–29.

[8] Xu, W.; Wang, J. L.; Ding, F.; Chen, X. L.; Nasybulin, E.; Zhang, Y. H.; Zhang, J. G. Lithium metal anodes for rechargeable batteries. *Energy Environ. Sci.* **2014**, *7*, 513–537.

[9] Tarascon, J. M.; Armand, M. Issues and challenges facing rechargeable lithium batteries. *Nature* **2001**, *414*, 359–367.

[10] Balakrishnan, P. G.; Ramesh, R.; Prem Kumar, T. Safety mechanisms in lithium-ion batteries. *J. Power Sources* **2006**, *155*, 401–414.

[11] Gordon, I. A. J.; Grugeon, S.; Takenouti, H.; Tribollet, B.; Armand, M.; Davoisne, C.; Débart, A.; Laruelle, S. Electrochemical impedance spectroscopy response study of a commercial graphite-based negative electrode for Li-ion batteries as function of the cell state of charge and ageing. *Electrochim. Acta* **2017**, *223*, 63–73.

[12] Wang, C.; Wang, F. X.; Zhao, Y. J.; Li, Y. H.; Yue, Q.; Liu, Y. P.; Liu, Y.; Elzatahry, A. A.; Al-Enizi, A.; Wu, Y. P. et al. Hollow TiO_{2-X} porous microspheres composed of well-crystalline nanocrystals for high-performance lithium-ion batteries. *Nano Res.* **2016**, *9*, 165–173.

[13] Yang, J. L.; Wu, Q. L.; Yang, X. F.; He, S. M.; Khan, J.; Meng, Y. Y.; Zhu, X. M.; Tong, S. F.; Wu, M. M. Chestnut-like TiO_2@α-Fe_2O_3 core–shell nanostructures with abundant interfaces for efficient and ultralong life lithium-ion storage. *ACS Appl. Mater. Interfaces* **2017**, *9*, 354–361.

[14] You, H. L.; Wu, Q. L.; Li, J. D.; He, S. M.; Li, X. H.; Yang, X. F.; Yang, J. L.; Meng, Y. Y.; Tong, S. F.; Wu, M. M. Hollow nanocubes constructed from <001> oriented anatase TiO_2 nanoarrays: Topotactic conversion and fast lithium-ion storage. *CrystEngComm* **2017**, *19*, 2456–2463.

[15] Wu, Y. Z.; Meng, J. S.; Li, Q.; Niu, C. J.; Wang, X. P.; Yang, W.; Li, W.; Mai, L. Q. Interface-modulated fabrication of hierarchical yolk–shell Co_3O_4/C dodecahedrons as stable anodes for lithium and sodium storage. *Nano Res.* **2017**, *10*, 2364–2376.

[16] Wang, H. G.; Wang, G. S.; Yuan, S.; Ma, D. L.; Li, Y.; Zhang, Y. Fe_3O_4-nanoparticle-decorated TiO_2 nanofiber hierarchical heterostructures with improved lithium-ion battery performance over wide temperature range. *Nano Res.* **2015**, *8*, 1659–1668.

[17] Dai, C. G.; Ye, J.; Zhao, S. Y.; He, P.; Zhou, H. S. Fabrication of high-energy Li-ion cells with $Li_4Ti_5O_{12}$ microspheres as anode and $0.5Li_2MnO_3{\cdot}0.5LiNi_{0.4}Co_{0.2}Mn_{0.4}O_2$ microspheres as cathode. *Chem. Asian J.* **2016**, *11*, 1273–1280.

[18] Ai, W.; Jiang, J.; Zhu, J. H.; Fan, Z. X.; Wang, Y. L.; Zhang, H.; Huang, W.; Yu, T. Supramolecular polymerization promoted *in situ* fabrication of nitrogen-doped porous graphene sheets as anode materials for Li-ion batteries. *Adv. Energy Mater.* **2015**, *5*, 1500559.

[19] Ai, W.; Luo, Z. M.; Jiang, J.; Zhu, J. H.; Du, Z. Z.; Fan, Z. X.; Xie, L. H.; Zhang, H.; Huang, W.; Yu, T. Nitrogen and sulfur codoped graphene: Multifunctional electrode materials for high-performance Li-ion batteries and oxygen reduction reaction. *Adv. Mater.* **2014**, *26*, 6186–6192.

[20] Lui, G.; Li, G.; Wang, X. L.; Jiang, G. P.; Lin, E.; Fowler, M.; Yu, A. P.; Chen, Z. W. Flexible, three-dimensional ordered macroporous TiO_2 electrode with enhanced electrode–electrolyte interaction in high-power Li-ion batteries. *Nano Energy* **2016**, *24*, 72–77.

[21] Chu, S. Y.; Zhong, Y. J.; Cai, R.; Zhang, Z. B.; Wei, S. Y.; Shao, Z. P. Mesoporous and nanostructured TiO_2 layer with ultra-high loading on nitrogen-doped carbon foams as flexible and free-standing electrodes for lithium-ion batteries. *Small* **2016**, *12*, 6724–6734.

[22] Ren, Y.; Hardwick, L. J.; Bruce, P. G. Lithium intercalation into mesoporous anatase with an ordered 3D pore structure. *Angew. Chem., Int. Ed.* **2010**, *49*, 2570–2574.

[23] Huang, S. Z.; Zhang, L.; Lu, X. Y.; Liu, L. F.; Liu, L. X.; Sun, X. L.; Yin, Y.; Oswald, S.; Zou, Z. Y.; Ding, F. et al. Tunable pseudocapacitance in 3D $TiO_{2-\delta}$ nanomembranes enabling superior lithium storage performance. *ACS Nano* **2017**, *11*, 821–830.

[24] Chattopadhyay, S.; Maiti, S.; Das, I.; Mahanty, S.; De, G. Electrospun TiO_2–rGO composite nanofibers with ordered mesopores by molecular level assembly: a high performance anode material for lithium-ion batteries. *Adv. Mater. Interfaces* **2016**, *3*, 1600761.

[25] Zhang, Y. Y.; Tang, Y. X.; Li, W. L.; Chen, X. D. Nanostructured TiO_2-based anode materials for high-performance rechargeable lithium-ion batteries. *ChemNanoMat* **2016**, *2*, 764–775.

[26] Kavan, L. Lithium insertion into TiO_2 (anatase): Electrochemistry, Raman spectroscopy, and isotope labeling. *J Solid State Electrochem.* **2014**, *18*, 2297–2306.

[27] Reddy, M. V.; Subba Rao, G. V.; Chowdari, B. V. R. Metal oxides and oxysalts as anode materials for Li ion batteries. *Chem. Rev.* **2013**, *113*, 5364–5457.

[28] Guo, Y. G.; Hu, Y. S.; Maier, J. Synthesis of hierarchically mesoporous anatase spheres and their application in lithium batteries. *Chem. Commun.* **2006**, 2783–2785.

[29] Zhao, Z. H.; Tian, J.; Sang, Y. H.; Cabot, A.; Liu, H. Structure, synthesis, and applications of TiO_2 nanobelts. *Adv. Mater.* **2015**, *27*, 2557–2582.

[30] Chen, J.; Zhang, Y.; Zou, G. Q.; Huang, Z. D.; Li, S. M.; Liao, H. X.; Wang, J. F.; Hou, H. S.; Ji, X. B. Size-tunable olive-like anatase TiO_2 coated with carbon as superior anode for sodium-ion batteries. *Small* **2016**, *12*, 5554–5563.

[31] Jiang, C. H.; Wei, M. D.; Qi, Z. M.; Kudo, T.; Honma, I.; Zhou, H. S. Particle size dependence of the lithium storage capability and high rate performance of nanocrystalline anatase TiO_2 electrode. *J. Power Sources* **2007**, *166*, 239–243.

[32] Shin, J. Y.; Samuelis, D.; Maier, J. Sustained lithium-storage performance of hierarchical, nanoporous anatase TiO_2 at high rates: Emphasis on interfacial storage phenomena. *Adv. Funct. Mater.* **2011**, *21*, 3464–3472.

[33] Zhao, K. N.; Zhang, L.; Xia, R.; Dong, Y. F.; Xu, W. W.; Niu, C. J.; He, L.; Yan, M. Y.; Qu, L. B.; Mai, L. Q. SnO_2 quantum dots@graphene oxide as a high-rate and long-life anode material for lithium-ion batteries. *Small* **2016**, *12*, 588–594.

[34] Tian, M.; Wang, W.; Liu, Y.; Jungjohann, K. L.; Thomas Harris, C.; Lee, Y. C.; Yang, R. G. A three-dimensional carbon nano-network for high performance lithium ion batteries. *Nano Energy* **2015**, *11*, 500–509.

[35] Zhu, Q.; Wu, P.; Zhang, J.; Zhang, W.; Zhou, Y.; Tang, Y.; Lu, T. Cyanogel-derived formation of 3D nanoporous SnO_2–M_xO_y (M=Ni, Fe, Co) hybrid networks for high-performance lithium storage. *ChemSusChem* **2015**, *8*, 131–137.

[36] An, Q. Y.; Wei, Q. L.; Zhang, P. F.; Sheng, J. Z.; Hercule, K. M.; Lv, F.; Wang, Q. Q.; Wei, X. J.; Mai, L. Q. Three-dimensional interconnected vanadium pentoxide nanonetwork cathode for high-rate long-life lithium batteries. *Small* **2015**, *11*, 2654–2660.

[37] Magasinski, A.; Dixon, P.; Hertzberg, B.; Kvit, A.; Ayala, J.; Yushin, G. High-performance lithium-ion anodes using a hierarchical bottom-up approach. *Nat. Mater.* **2010**, *9*, 353–358.

[38] Hengerer, R.; Kavan, L.; Krtil, P.; Grätzel, M. Orientation dependence of charge-transfer processes on TiO_2 (anatase) single crystals. *J. Electrochem. Soc.* **2000**, *147*, 1467–1472.

[39] Wu, Q. L.; Yang, X. F.; Zhou, W. Z.; Gao, Q.; Lu, F. Q.; Zhuang, J. L.; Xu, X. F.; Wu, M. M.; Fan, H. J. "Isofacet" anatase TiO_2 microcages: Topotactic synthesis and ultrastable Li-ion storage. *Adv. Mater. Interfaces* **2015**, *2*, 1500210.

[40] Wu, Q. L.; Xu, J. G.; Yang, X. F.; Lu, F. Q.; He, S. M.; Yang, J. L.; Fan, H. J.; Wu, M. M. Ultrathin anatase TiO_2 nanosheets embedded with TiO_2-B nanodomains for lithium-ion storage: Capacity enhancement by phase

boundaries. *Adv. Energy Mater.* **2015**, *5*, 1401756.

[41] Yang, X. F.; Karthik, C.; Li, X. Y.; Fu, J. X.; Fu, X. H.; Liang, C. L.; Ravishankar, N.; Wu, M. M.; Ramanath, G. Oriented nanocrystal arrays of selectable polymorphs by chemical sculpture. *Chem. Mater.* **2009**, *21*, 3197–3201.

[42] Tsai, C. C.; Teng, H. Structural features of nanotubes synthesized from NaOH treatment on TiO_2 with different post-treatments. *Chem. Mater.* **2006**, *18*, 367–373.

[43] Yang, J. J.; Jin, Z. S.; Wang, X. D.; Li, W.; Zhang, J. W.; Zhang, S. L.; Guo, X. Y.; Zhang, Z. J. Study on composition, structure and formation process of nanotube $Na_2Ti_2O_4(OH)_2$. *Dalton Trans.* **2003**, 3898–3901.

[44] Wu, Q. L.; Yang, X. F.; Liu, J.; Nie, X.; Huang, Y. L.; Wen, Y. P.; Khan, J.; Khan, W. U.; Wu, M. M.; An, T. C. Topotactic growth, selective adsorption, and adsorption-driven photocatalysis of protonated layered titanate nanosheets. *ACS Appl. Mater. Interfaces* **2014**, *6*, 17730–17739.

[45] Chen, Q.; Mogilevsky, G.; Wagner, G. W.; Forstater, J.; Kleinhammes, A.; Wu, Y. Active anatase (001)-like surface of hydrothermally synthesized titania nanotubes. *Chem. Phys. Lett.* **2009**, *482*, 134–138.

[46] Mogilevsky, G.; Chen, Q.; Kulkarni, H.; Kleinhammes, A.; Mullins, W. M.; Wu, Y. Layered nanostructures of delaminated anatase: Nanosheets and nanotubes. *J. Phys. Chem. C* **2008**, *112*, 3239–3246.

[47] Lu, H. Q.; Zhao, J. H.; Li, L.; Zheng, J. F.; Zhang, L. X.; Gong, L. M.; Wang, Z. J.; Zhu, Z. P. A systematic study on evolution mechanism of titanate nanostructures in the hydrothermal process. *Chem. Phys. Lett.* **2011**, *508*, 258–264.

[48] Nakahira, A.; Kubo, T.; Numako, C. Formation mechanism of TiO_2-derived titanate nanotubes prepared by the hydrothermal process. *Inorg. Chem.* **2010**, *49*, 5845–5852.

[49] Kasuga, T.; Hiramatsu, M.; Hoson, A.; Sekino, T.; Niihara, K. Titania nanotubes prepared by chemical processing. *Adv. Mater.* **1999**, *11*, 1307–1311.

[50] Zhang, H. B.; Cao, L. X.; Liu, W.; Su, G. A new ion exchange behavior of protonated titanate nanotubes after deprotonation and the study on their morphology and optical properties. *Appl. Surf. Sci.* **2012**, *259*, 610–615.

[51] Bavykin, D. V.; Friedrich, J. M.; Walsh, F. C. Protonated titanates and TiO_2 nanostructured materials: Synthesis, properties, and applications. *Adv. Mater.* **2006**, *18*, 2807–2824.

[52] Kim, S.; Kim, M.; Hwang, S. H.; Lim, S. K. Effects of hydrothermal temperature and acid concentration on the transition from titanate to titania. *J. Ind. Eng. Chem.* **2012**, *18*, 1141–1148.

[53] Wang, C. H.; Zhang, X. T.; Zhang, Y. L.; Jia, Y.; Yang, J. K.; Sun, P. P.; Liu, Y. C. Hydrothermal growth of layered titanate nanosheet arrays on titanium foil and their topotactic transformation to heterostructured TiO_2 photocatalysts. *J. Phys. Chem. C* **2011**, *115*, 22276–22285.

[54] Li, N.; Zhang, L. D.; Chen, Y. Z.; Fang, M.; Zhang, J. X.; Wang, H. M. Highly efficient, irreversible and selective ion exchange property of layered titanate nanostructures. *Adv. Funct. Mater.* **2012**, *22*, 835–841.

[55] Kim, C.; Buonsanti, R.; Yaylian, R.; Milliron, D. J.; Cabana, J. Carbon-free TiO_2 battery electrodes enabled by morphological control at the nanoscale. *Adv. Energy Mater.* **2013**, *3*, 1286–1291.

[56] Rhee, O.; Lee, G.; Choi, J. Highly ordered TiO_2 microcones with high rate performance for enhanced lithium-ion storage. *ACS Appl. Mater. Interfaces* **2016**, *8*, 14558–14563.

[57] Tang, Y. X.; Zhang, Y. Y.; Deng, J. Y.; Wei, J. Q.; Tam, H. L.; Chandran, B. K.; Dong, Z. L.; Chen, Z.; Chen, X. D. Mechanical force-driven growth of elongated bending TiO_2-based nanotubular materials for ultrafast rechargeable lithium ion batteries. *Adv. Mater.* **2014**, *26*, 6111–6118.

[58] Wang, Z. Y.; Lou, X. W. TiO_2 nanocages: Fast synthesis, interior functionalization and improved lithium storage properties. *Adv. Mater.* **2012**, *24*, 4124–4129.

[59] Yue, W. B.; Xu, X. X.; Irvine, J. T. S.; Attidekou, P. S.; Liu, C.; He, H. Y.; Zhao, D. Y.; Zhou, W. Z. Mesoporous monocrystalline TiO_2 and its solid-state electrochemical properties. *Chem. Mater.* **2009**, *21*, 2540–2546.

[60] Chen, J. S.; Lou, X. W. Anatase TiO_2 nanosheet: An ideal host structure for fast and efficient lithium insertion/extraction. *Electrochem. Commun.* **2009**, *11*, 2332–2335.

[61] Uchaker, E.; Cao, G. Z. Mesocrystals as electrode materials for lithium-ion batteries. *Nanotoday* **2014**, *9*, 499–524.

[62] Wang, J.; Polleux, J.; Lim, J.; Dunn, B. Pseudocapacitive contributions to electrochemical energy storage in TiO_2 (anatase) nanoparticles. *J. Phys. Chem. C* **2007**, *111*, 14925–14931.

[63] Han, H.; Song, T.; Lee, E. K.; Devadoss, A.; Jeon, Y.; Ha, J.; Chung, Y. C.; Choi, Y. M.; Jung, Y. G.; Paik, U. Dominant factors governing the rate capability of a TiO_2 nanotube anode for high power lithium ion batteries. *ACS Nano* **2012**, *6*, 8308–8315.

[64] Wang, J.; Ran, R.; Tade, M. O.; Shao, Z. P. Self-assembled mesoporous TiO_2/carbon nanotube composite with a three-dimensional conducting nanonetwork as a high-rate anode material for lithium-ion battery. *J. Power Sources* **2014**, *254*, 18–28.

[65] Yi, T. F.; Xie, Y.; Jiang, L. J.; Shu, J.; Yue, C. B.; Zhou, A. N.; Ye, M. F. Advanced electrochemical properties of Mo-doped $Li_4Ti_5O_{12}$ anode material for power lithium ion battery. *RSC Adv.* **2012**, *2*, 3541–3547.

[66] Cheng, Y. H.; Chen, Z.; Wu, H. B.; Zhu, M. F.; Lu, Y. F. Ionic liquid-assisted synthesis of TiO_2-carbon hybrid nanostructures for lithium-ion batteries. *Adv. Funct. Mater.* **2016**, *26*, 1338–1346.

[67] Liu, H.; Li, W.; Shen, D. K.; Zhao, D. Y.; Wang, G. X. Graphitic carbon conformal coating of mesoporous TiO_2 hollow spheres for high-performance lithium ion battery anodes. *J. Am. Chem. Soc.* **2015**, *137*, 13161–13166.

[68] Li, Y. M.; Shen, J. R.; Li, J. J.; Liu, S. M.; Yu, D. L.; Xu, R. C.; Fu, W. F.; Lv, X. J. Constructing a novel strategy for carbon-doped TiO_2 multiple-phase nanocomposites toward superior electrochemical performance for lithium ion batteries and the hydrogen evolution reaction. *J. Mater. Chem. A* **2017**, *5*, 7055–7063.

[69] Zhu, H. W.; Jing, Y. K.; Pal, M.; Liu, Y. P.; Liu, Y.; Wang, J. X.; Zhang, F.; Zhao, D. Y. Mesoporous TiO_2@N-doped carbon composite nanospheres synthesized by the direct carbonization of surfactants after sol-gel process for superior lithium storage. *Nanoscale* **2017**, *9*, 1539–1546.